Nanoscale

Accepted Manuscript

This article can be cited before page numbers have been issued, to do this please use: D. Placente, J. M. Ruso, M. Baldini, J. M. Sieben, J. A. Laiuppa, G. E. Santillán and P. V. V. Messina, *Nanoscale*, 2019, DOI: 10.1039/C9NR01236B.

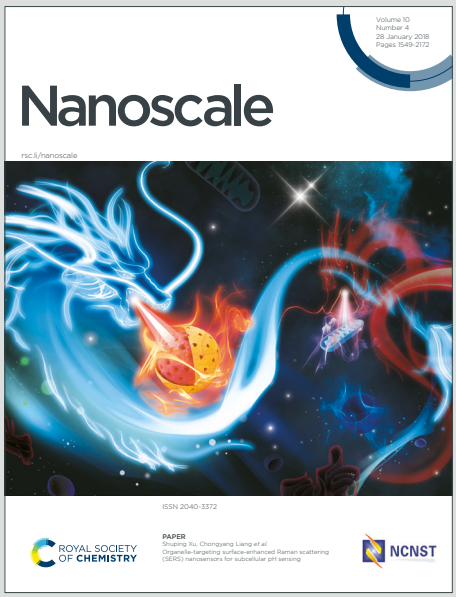

ROYAL SOCIETY OF CHEMISTRY

rsc.li/nanoscale

View Article Online
DOI: 10.1039/C9NR01236B

Self-fluorescent Antibiotic MoO_x-Hydroxyapatite: A Nano- theranostic Platform for Bone Infection Therapies

Damián Placente [a], *Juan. M. Ruso* [b], *Mónica Baldini* [c], *Juan A. Laiuppa* [c,d§], *Juan M. Sieben* [e§], *Graciela E. Santillán* [c,d], *Paula V. Messina* [a]*

(a) INQUISUR – CONICET, Department of Chemistry, Universidad Nacional del Sur, B8000CPB, Bahía Blanca, Argentina. (b) Soft Matter and Molecular Biophysics Group, Department of Applied Physics, University of Santiago de Compostela, 15782 Santiago de Compostela, Spain (c) Department of Biology, Biochemistry and Pharmacy, Universidad Nacional del Sur, B8000ICN, Bahía Blanca, Argentina. (d) INBIOSUR – CONICET. (e) INIEC – CONICET, Department of Chemistry Engineering, Universidad Nacional del Sur, B8000CPB Bahía Blanca, Argentina

* Author to whom correspondence should be addressed. Tel: +54 291 4595159. Fax: +54 291 4595160. Electronic mail: pmessina@uns.edu.ar.

§ Juan A. Laiuppa and Juan M. Sieben have contributed equally to this work.

View Article Online
DOI: 10.1039/C9NR01236B

Abstract. Nowadays, the repair of large-size bone defects represents a huge medical challenge. A line of attack is the construction of advanced biomaterials having multifunctional properties. In this work, we show the creation of biocompatible MoO_x-hydroxyapatite nanoparticles (nano-HA/MoO_x) that simultaneously exhibit self-activated fluorescence and antibiotic skills. Along this text, we demonstrate that the insertion of molybdenum, an essential trace element, into the non-stoichiometric calcium deficient hydroxyapatite lattice generates intrinsic electronic point defects that exacerbate its epifluorescence blue emission and provokes new red emissions; preserving, always, its bioactivity. Furthermore, these point defects, acting as electron acceptors, stimulate the materials' biological redox status and promote the death of pathogen microorganisms after its direct contact. A putative mechanism, by which bacteria lose electrons from their metabolic circuit that alter the function of their cytoplasmic membrane and potentially die, agrees to our results.

Our findings highlight the importance of tuning the electronic communications between biomaterial interfaces and biological units, and support the use of the self-fluorescent MoO_x-hydroxyapatite nanoparticles as fundamental building blocks for new real-time image platforms against bone infection.

View Article Online
DOI: 10.1039/C9NR01236B

Introduction

Bone is an organ designed to be meaningfully protected against external pathogens.[1] Nevertheless, to the same extent that repels infections, it resists therapies against them. Presently, notwithstanding the progresses in the field of implantable materials and the application of the best practice in surgical management, a significant proportion of current medical applied devices become contaminated and colonized by bacteria.[2] Consequently, the problem of orthopaedics device-related infections remains a challenge for clinicians. Traditional treatments, like radical debridement, revision surgery and prolonged antibiotic therapy against resistant bacteria, often result in significant economic costs and the risk of lifelong functional impairment for the patient, turning out the treatment to be worse than the initial disease.[3-5]

Along this line, the development of new approaches specifically designed to remove pathogenic microorganisms from orthopaedic devices is a modern necessity, and nano-particulate platforms hold the greatest potential since they provide the option of multiple functions integrated into a single system. In preceding investigations, we have formulated original bone mimetic networks based on hydroxyapatite nano-rods (nano-HA). Nano-HA were precisely designed to attain, all together, tissue regeneration[6-8] and defence against drug-resistant bone infection strains.[9, 10] In this investigation, we have improved our design by spawning chemical and physical changes on nano-HA using molybdenum oxides, MoO_x. Molybdenum (Mo) is an essential trace element[11] and its oxides are amongst the highest adaptable and functional optical and electronic compounds.[12] Therefore, well-recognized applications in sensors, field emission devices, thermal materials, chromogenic and electrochromic tools are reported.[12] Likewise, antimicrobial properties have been also associated to Mo and MoO_x nanoparticles.[13, 14]

View Article Online
DOI: 10.1039/C9NR01236B

Here, we have confirmed that self-activated fluorescence properties[15] can be induced by the merge of MoO_x into HA crystals; offering an extra-added value to the already demonstrated bone-repair and antimicrobial skills of our nano-platforms. Compared to other techniques, fluorescence imaging is advantageous because of its highly sensitivity, minimal invasiveness, and safety; moreover, it is of the preferred methods to observe biological events.[16] Self-activated fluorescent nano-HA/MoO_x systems may be promising platforms for bio-imaging due to their good optical properties and their substantially reduced toxicity. In addition, they can proffer protection and tissue regeneration abilities. In this sense, systems biocompatibility and antibacterial activity were validated by the interaction with primary cells cultures of rat calvarial osteoblasts and drug-resistance strains responsible to clinical bone infections: *Staphylococcus aureus* and *Pseudomona aeruginosa*. It was proposed a putative mechanism, by which the disruption of metabolic electron transference along prokaryote cytoplasmic membrane after interaction with the inorganic surface of nano-HA/MoO_x systems would be the potential route of annihilation.

Experimental

Materials and methods

Triblock poly(ethylene glycol)-poly(propylene glycol)-poly(ethylene glycol) copolymer Pluronic® F-127 ($EO_{102}PO_{70}EO_{102}$, CAS n° 9003-11-6, BioReagent, Sigma - Aldrich); polyethylene glycol (20) sorbitan monostearate (Tween® 60, CAS n° 9005-67-8, Sigma - Aldrich); sodium phosphate tribasic dodecahydrate ($Na_3PO_4 \cdot 12H_2O$, CAS n° 10101-89-0, Sigma - Aldrich); calcium chloride ($CaCl_2$, CAS n°10043-52-4, Sigma - Aldrich); phosphomolybdic acid hydrate ($H_3[P(Mo_3O_{10})_4] \cdot xH_2O$, CAS n°51429-74-4, Sigma –

View Article Online
DOI: 10.1039/C9NR01236B

Aldrich); phosphate buffer saline (PBS tablets, Na_2HPO_4 / NaH_2PO_4, Sigma - Aldrich); ethanol (EtOH, CAS n° 64-17-5, Sigma – Aldrich); Neutral Red dye ($C_{15}H_{17}ClN_4$, CAS n° 553-24-2, BioReagent, Sigma - Aldrich); 2,3,5-Triphenyl-2H-tetrazolium chloride 98% ($C_{19}H_{15}ClN_4$, CAS n° 298-96-4, Sigma - Aldrich) and L-Ascorbic acid redox probe ($C_6H_8O_6$, CAS n°A92902 Sigma - Aldrich) were used without further purification. Determination of phosphomolybdic acid (PMA) total hydration water (x = 28 molecules) was performed accordingly to the volumetric Karl Fischer titration method following the active standard ASTM E203-16.[17] For solutions preparation, only Milli-Q water was used.

Polymeric micelle-templating synthesis of HA and nano-HA/MoO_x platforms

Hydroxyapatite nanoparticles, nano-HA, were prepared according to a modification of the method proposed by F. Ye *et al.*[18] using a mixture of non-ionic surfactants as template. First 0.2900 g of Pluronic® F-127 were dissolved in 10 mL of a water / EtOH equivolumetric solution after vigorous sonication. Then, a second solution containing 0.1310 g of Tween®60, 3.8012 g of $Na_3PO_4 \cdot 12H_2O$ and 20 mL of Milli-Q water was prepared; the constituents were magnetically stirred at 500 rpm until completely dissolution at room temperature (RT). Following, both solutions were mixed together and then continuously stirred at 500 rpm for one hour at RT. Subsequently, 0.01675 mol of Ca^{2+} ions (5 mL of a 37 wt.% $CaCl_2$ aqueous solution, pH = 9) was slowly added, drop wise, while stirring. After the integration of all reactants, the resulting gel was autoclaved during 48 h at 100 °C. To finish, the powders were filtered and properly washed with Milli-Q water. Surfactant was completely removed by calcination at 400 °C during 3 h under air flux.[6]

View Article Online
DOI: 10.1039/C9NR01236B

Modified Incipient Wetness Impregnation Method[19] was used to prepared nano-HA/MoO_x platforms. Accordingly, 100 mg of the previously described nano-HA were dispersed in 50 mL of Milli-Q water after strong sonication during 45 min. Next, the required amounts of $H_3[P(Mo_3O_{10})_4]\cdot 28H_2O$ were water dissolved and 10 mL of 4, 2, 1 and 0.5 wt.% of PMA aqueous solutions were added to each nano-HA dispersion. Mixtures were magnetically stirred at 500 rpm during 45 min at RT. Finalizing, reaction vessels were left at 100 °C in an autoclave throughout 24 h; the obtained nano-HA/MoO_x solid materials were properly filtered and washed with Milli-Q water. The pHs of solutions were measured throughout the experiment by means of an ION 510 Benchtop Meter (OAKTON Instruments). UV-vis spectrophotometric inspection was performed at RT using an Agilent Cary 60 spectrophotometer with a 1 cm path length quartz cell. Four materials were obtained and denoted accordingly to the initial synthesis solutions PMA / nano-HA weight ratio: 4/1 (HA/MoO_x (I)); 2/1 (HA/MoO_x (II)); 1/1 (HA/MoO_x (III)) and 1/2 (HA/MoO_x (IV) respectively.

Microstructural and morphological characterization

High resolution transmission electron microscopy (H-TEM) microphotographs were acquired using a Libra 200 FE OMEGA microscope working at 200 kV of operating voltage that corresponds to a maximum magnification of 1 000 000 ×. Powdered samples were situated on carbon supports of 2000 mesh as required and observations were made in a bright field. Selected-area electron diffraction (SAED) patterns were extracted from the Fourier transform (FFT) of H-TEM microphotographs by digitalized image processing using a free software, Image J.[20]

View Article Online
DOI: 10.1039/C9NR01236B

Topographical characterization was performed using a field emission scanning electron microscopy (FE-SEM) ZEISS ULTRA PLUS coupled to an X-ray energy-dispersive (EDX) spectrophotometer that enables elemental chemical microanalysis. Images were acquired with a secondary electron detector (In lens) operated at an accelerating voltage (EHT) of 3.00 kV and at a working distance (WD) resolution of 2.1 nm. Local compensation of charge was achieved by injecting nitrogen gas.

X-ray powder diffraction (XRD) data were acquired with a Philips PW 1710 diffractometer associated to a Cu Kα radiation source (λ = 1.5418 nm) and a graphite monochromator operated at 45 kV, 30 mA, and RT. Joint Committee on Powder Diffraction Standards cards (JCPDS file #09-0432) and RRUFF database files[21] (R060180, R100180) were used as references. Lattice geometry parameters (*a, b, c)* and volume of the direct unit cell *(V)* were computed by Rietveld refinement using Rietica v4.2 free software package.[22] Molecular modelling were performed by a combined method for *ab initio* structure solution from powder diffraction data[23] using Endeavour software package (free demo version). For details please refers to electronic supplementary information, ESI, **sections ESI-1** and **ESI-2**.

Electroactive and photoactive molecular characterization

Electroactive behavior of nano-HA/MoO_x platforms were tested against L-Ascorbic acid (AA) redox probe (10.0 mM, PBS buffered solution) following a previous descript procedure.[9] Conventional three-compartment glass cells were used to run the electrochemical experiments at RT with a Princeton Applied Research VersaSTAT 3 potentiostat / galvanostat. A platinum (Pt) wire was used as the counter electrode, while a saturated calomel electrode (SCE, +0.241 vs. NHE) served as reference. Nano-HA/MoOx

View Article Online
DOI: 10.1039/C9NR01236B

modified electrodes were prepared accordingly to Andres *et al*.[9] Cyclic voltammograms (CV) were recorded at different scan rates, ranging from 10 to 500 mV s^{-1}. The semi-integral convolution of the voltammetric data was done using the eL-ChemViewer based freeware package.[24] The scan rate dependence with the peak heights for the anodic wave was evaluated by the Randles-Ševčik equation[25] and the heterogeneous rate constant ($k_{(E)}$) for quasi-reversible systems on the positive sweep was expressed according to Deakin *et al*.[26], details are shown in section **ESI-3**.

Optoelectronic properties of all samples were evaluated by recording their UV-vis and fluorescence spectra at RT using an Agilent Cary 60 UV-Vis spectrophotometer and a JASCO FP-6500 scanning spectrofluorometer, respectively; in both cases, a 1 cm path length quartz cell was used. Fluorescence determinations were achieved using 5 nm of band width both for excitation and emission purposes, a response of 0.2 seconds and a scanning speed of 5000 nm /min. Both spectra were recorded after the sonication of particles (1 mg / mL) in PBS to yield homogeneous dispersions. PBS solution was used as blank. The optical band gap energies (E_g) of polycrystalline nano-HA and nano-HA/MoO_x platforms were estimated from the sharply increasing absorption region according to Tauc and Menth's law[27]; for details please refer to section **ESI-4**.

To evaluate the epi-fluorescence of nano-HA and nano-HA/MoO_x samples, homogeneous material dry coatings[6] were observed in a Nikon Eclipse TE300 inverted microscope. Equipment was provided with an ANDOR Neo/Zyla B&W and a DS Fi2 color digital cameras for fluorescent and bright field images respectively. Photographs were acquired using no filters (for bright field/phase contrast), and Chroma 8300 filter set with single

View Article Online
DOI: 10.1039/C9NR01236B

band exciters (DAPI (λ_{EX} = 360 nm /40x), FITC (λ_{EX} = 492 nm /18x) and Texas Red (λ_{EX} = 572 nm /23x)). Uncoated wells were used as control, C.

Cellular viability and antimicrobial activity

Viability of nano-HA and HA/MoO_x powders were tested in the presence of primary cells cultures of rat calvarial osteoblast (rOBs) as previously described[28]; for more information please refer to section **ESI-5**. Cell viability estimation was done following the Neutral Red uptake assay[29], and confirmed by morphological observation using a Nikon Eclipse TE 300 microscope coupled to a Nikon Digital Sight DS U2 camera. Primary rOBs cultured in absence of material were used as control, C. Cytomorphometric analysis was done using the free Image J[20] software accordingly to Foldberg *et al.* methodology[30]; details are shown in **ESI-5**.

Antimicrobial effects of nano-HA and HA/MoO_x samples were tested against two bacterial strains representing a clinically relevant spectrum of microorganisms.[10] Gram-negative, *Pseudomona aeruginosa* (*P. aeruginosa*, ATCC 27853) and, Gram-positive, *Staphylococcus aureus* (*S. aureus*, ATCC 29213) bacteria were isolated and stored at Microbiology Chair, Department of Biology, Biochemistry and Pharmacy of the Universidad Nacional del Sur, Argentina. Bacteria were cultured at 37 °C and allowed to mature overnight to ensure they were growing exponentially before their use. Following, 100 μL from a stock dispersion equivalent to 0.5 McFarland turbidity standards, 10^6 colony formation units (CFU) / mL, were taken and placed in test tubes containing 50 and 100 mg / mL of the material to be investigated in a final volume of 5 mL of standard nutritive broth (Sigma-Aldrich, CAS no. 70122). Bacteria were exposed to nano-HA and HA/MoO_x

View Article Online
DOI: 10.1039/C9NR01236B

samples for 24 and 48 h with continuous stirring at 100 rpm in a rotary shaker (New Brunswick Scientific). After the samples contact time, 1 mL supernatants aliquots were taken and diluted as required accordingly to the method described by Miles *et al.*[31] From each of these serial dilutions, 1 mL was placed into sterile culture petri dishes (8.5 cm diameter) and then 20 mL of sterile plate count agar (reference n°1054630500, Merck) were poured over the sample. After agar solidification at RT, the plates were incubated for 24 h at 37 °C; those containing between 30 and 300 colonies were counted and multiplied by the proper dilution value to attain the final bacteria colony number. Results were expressed as percentage of bacteria colony counts reduction, $R\% = \left(\left(R_i - R_f\right)/R_i\right) \times 100$, where R_i and R_f are the initial and final bacterial amounts expressed in CFU/ mL. Microbial culture in absence of material was used as control, C. Examination of bacterial cytoplasmatic membrane integrity was performed by the colorimetric determination of reducing sugars with triphenyltetrazolium chloride accordingly to Mattson and Jensen methodology.[32] To detect the leakage of reducing sugars through the cytoplasmic membrane, the properly amounts of Mueller Hinton broth, materials and microorganisms were added to test tubes, achieving a final bacterial concentration of 10^6 CFU / mL, and 100 mg / mL of HA and HA/MoO_x nanoparticles. They were left in contact during 48 h and then the supernatants of all test tubes were centrifuged and separated. 1 mL of each supernatant was kept, and then used to test the presence of reducing sugars.[32] Results were expressed in % of leakage of reducing sugars, $\%RS = \left(\left(A_f - A_i\right)/A_f\right) \times 100$, where A_f and A_i are the final and initial solution absorbance read at 577 nm. Microbial culture in absence of material was used as control, C. Bacterial inspection was fulfilled by transmission electron microscopy (TEM) observations. For this experiment, 1 mL of

View Article Online
DOI: 10.1039/C9NR01236B

bacterial dispersion after 48 h of material contact was taken, fixed with glutaraldehyde solution (Grade I, 25% in H_2O solution, CAS N°111-30-8, Sigma-Aldrich), stained with a 2 wt.% uranyl acetate water solution (pH 4.2 to 4.5) and observed in a Philips CM-12 transmission electron microscope operated at 120 kV. Observations were made with a digital camera MEGA VIEW-II DOCU in a bright field; powdered samples were placed on cupper supports of 2000 mesh.

Statistical Analysis

All quantitative assessments were taken at least in triplicate and results were expressed as mean ± standard deviation (SD). Statistical analysis of data was realized by one factor analysis of variance (ANOVA). Student's t-test and probability values below 0.05 ($p < 0.05$) were considered as a significantly difference.

View Article Online
DOI: 10.1039/C9NR01236B

Results and discussion

Phosphate $(PO_4)^{3-}$ ions can be substituted by metal complexes like vanadate $(VO_4)^{3-}$ and molybdate $(MoO_4)^{2-}$ into the crystal lattice of calcium deficient nonstoichiometric hydroxyapatites, $Ca_{10-x}(HPO_4)_x(PO_4)_{6-x}(OH)_{2-x}$.[33] It would be expected that the modification of this active material by metallic doping would produce the "tuning" of multiple active sites. This hypothesis will be tested along the following sections.

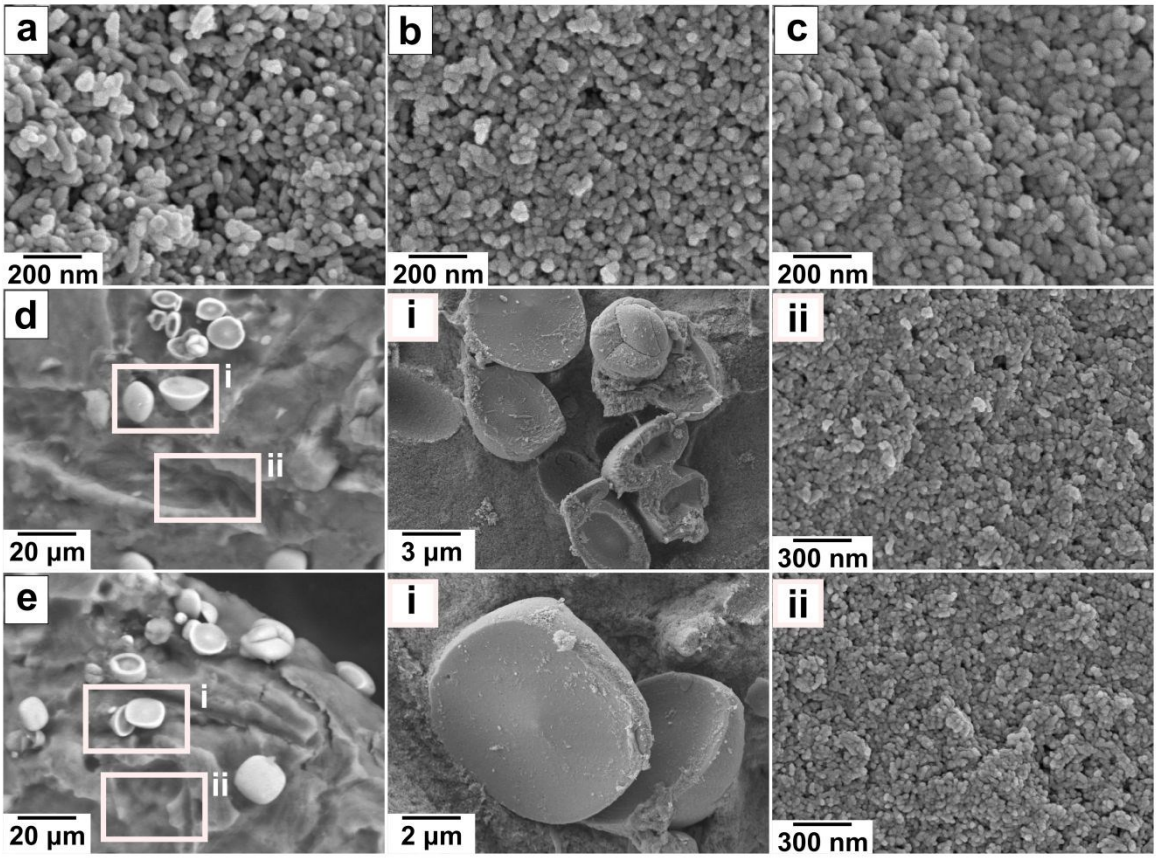

Figure 1, FE-SEM microphotographs of **(a)** HA, **(b)** HA/MoO_x (I), **(c)** HA/MoO_x (II), **(d)** HA/MoO_x (III) and **(e)** HA/MoO_x (IV). (i) rich-Mo deposits and (ii) HA nano-rods.

Nano-HA/MoO_x platforms: microstructural switch processing

Disruption of solid-state phase transformation and fluctuations of crystalline materials microstructure are directly related to ionic interaction or substitution.[34, 35] FE-SEM

View Article Online
DOI: 10.1039/C9NR01236B

microphotographs of HA/MoO_x powders are shown in **figure 1**. It can be seen that the HA/MoO_x (I) and HA/MoO_x (II) samples, **figures 1b-c**, exhibit a nano-structured network wrought by assemble of uniform rod-like nanoparticles with similar aspect ratios (length/diameter) than those observed in untreated HA, **figure 1a**. A slight reduction of rods' length was appreciated for both HA/MoO_x (III) and HA/MoO_x (IV) specimens; please refer to **table ESI9**. Energy-dispersive X-ray spectroscopy (EDX) measurements confirmed that un-substituted HA rod-like nanoparticles possess a Ca/P elemental ratio of about 1.52 that is characteristic of non-stoichiometric hydroxyapatite crystalline phase; spectrum is illustrated in **figure ESI6-a**. On contrary, elemental microanalysis of bulk HA/MoO_x (I-IV) samples revealed a superior Ca/P ratio compared to stoichiometric HA (Ca/P ≈ 1.67), in all cases elemental Mo were detected, **figures ESI6-b, ESI6-c**. For both HA/MoO_x (III) and HA/MoO_x (IV) specimens, the presence of spherical or semi-spherical deposits of large size onto HA nanostructured networks were found, **figures 1d-e**; EDX microanalysis exposed that they were constituted by a rich-molybdenum phase, **figure ESI6-c**.

Microcrystalline structure was verified after the inspection of H-TEM microphotographs and X-ray diffraction patterns, **figure 2**. Hydroxyapatite as well as the HA/MoO_x (I-II) specimens, **figures 2a-b**, showed the presence of defined crystalline rod-shaped nanoparticles, while HA/MoO_x (III) and HA/MoO_x (IV) samples displayed crystalline zones embedded in an amorphous matrix, **figures 2c-d**. In agreement to H-TEM results, XRD spectra, **figure 2e**, exhibited reflections associated to poor crystallized calcium deficient hydroxyapatite similar to that exist in biological specimens[36] and decreasing in intensity and crystallinity from sample II to IV. Additionally, HA/MoO_x (III) and HA/MoO_x (IV) powders exposed a second X-ray diffraction pattern configuration that was

View Article Online
DOI: 10.1039/C9NR01236B

identified as powellite, $Ca(MoO_4)$, ratifying the presence of a rich-molybdenum phase amalgamated with HA.

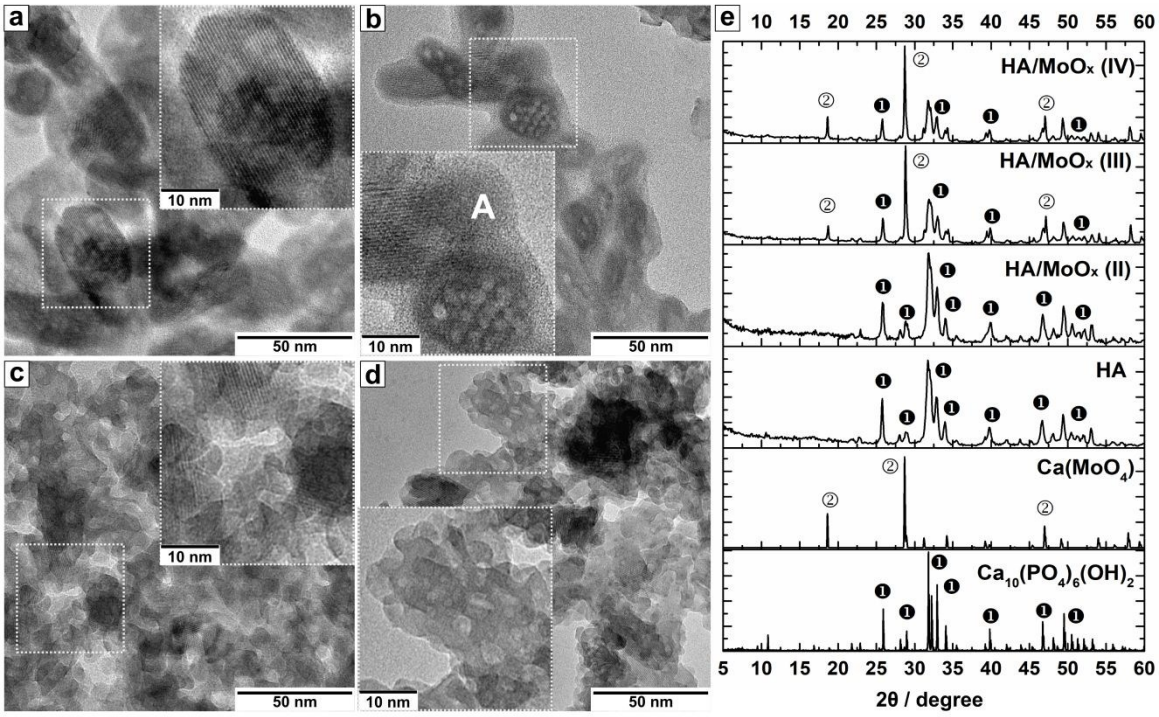

Figure 2, High resolution TEM microphotographs of **(a)** HA, **(b)** HA/MoO_x (II), **(c)** HA/MoO_x (III) and **(d)** HA/MoO_x (IV) samples. A: amorphous phase. In order to simplify the diagram and due to the morphological similitude between HA/MoOx (I) and HA/MoOx (II) samples, the HA/MoOx (I) photographs are not shown. **(e)** XRD patterns of HA/MoO_x powders; hydroxyapatite ($Ca_{10}(PO_4)_6(OH)_2$, R130713.9) and powellite ($Ca(MoO_4)$, R100180) from RRUFF database are used as references.[21]

A deep inspection of the selected-area electron diffraction (SAED) patterns for HA/MoO_x (III-IV) samples settled the presences of both HA and powellite phases in a complete communion inside the material structure, **figure 3**. SEAD arrays displayed a perfect hexagonal configuration, **figures 3a-i** and **3b-i,** which were indexed to HA (300) planes viewed along crystallography "*c*" direction and the characteristic tetragonal design of powellite (112) planes along "*b*" path, **figures 3a-ii** and **3b-ii.**

View Article Online
DOI: 10.1039/C9NR01236B

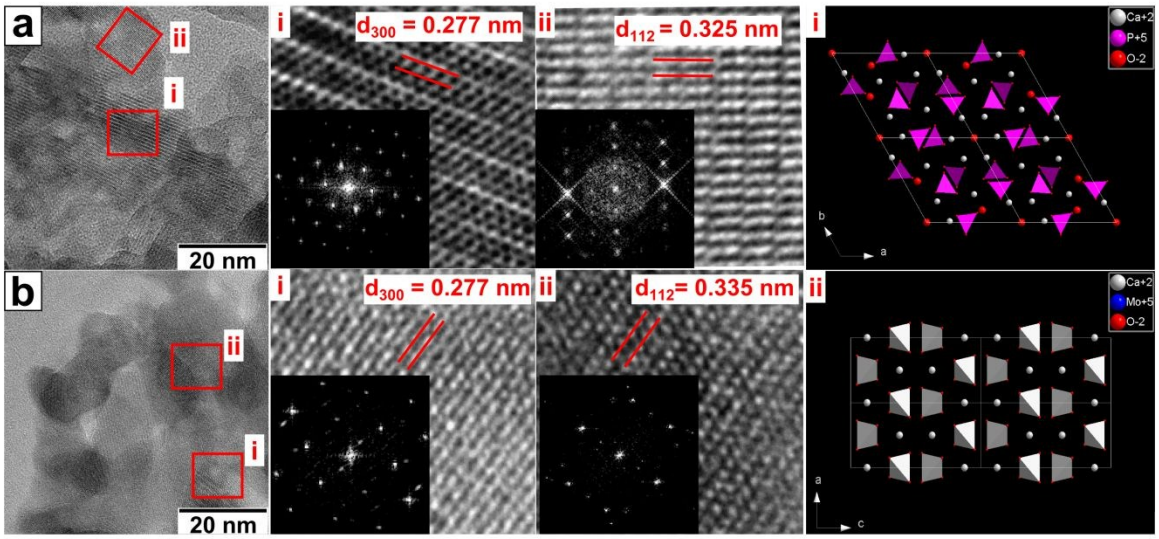

Figure 3, H-TEM of **(a)** HA/MoO_x (III) and **(b)** HA/MoO_x (IV) samples. Selected crystalline areas are signaled in red boxes. Selected-area electron diffraction (SAED) patterns were extracted from the Fourier transform (FFT) of H-TEM microphotographs by Image J[20] software processing and compared with theoretical direct unit cell structures generated by the *ab initio* method. [23] **(i)** Hydroxyapatite and **(ii)** powellite crystals planes.

Notwithstanding the resemblance of HA-XRD profiles in all samples, slight divergences were observed from a deeper examination of interplanar d-spacings. Semi-empiric *ab initio* molecular modeling, **figure 4**, and crystallographic parameters calculations were used to validate the distortion of HA direct unit cell and the possible incorporation of Mo atoms. Unmodified HA showed values of the lattice geometric parameters and of the unit direct cell volume, a = b = 9.439 Å; c = 6.914 Å; and 533.1 $Å^3$, comparable to reference standards (R130713.9)[21] and to previously obtained data[6, 8]; while for HA/MoO_x platforms, their magnitudes decreased always as we move from samples (I) - (IV), **table 1**. Obtained results were ascribed to the substitution of groups $(PO_4)^{3-}$ for $(MoO_4)^{2-}$. Both ions have a tetrahedral spatial arrangement and a similar topological polar surface[37, 38], which cause a compatible stereochemically and electrostatically replacement.

View Article Online
DOI: 10.1039/C9NR01236B

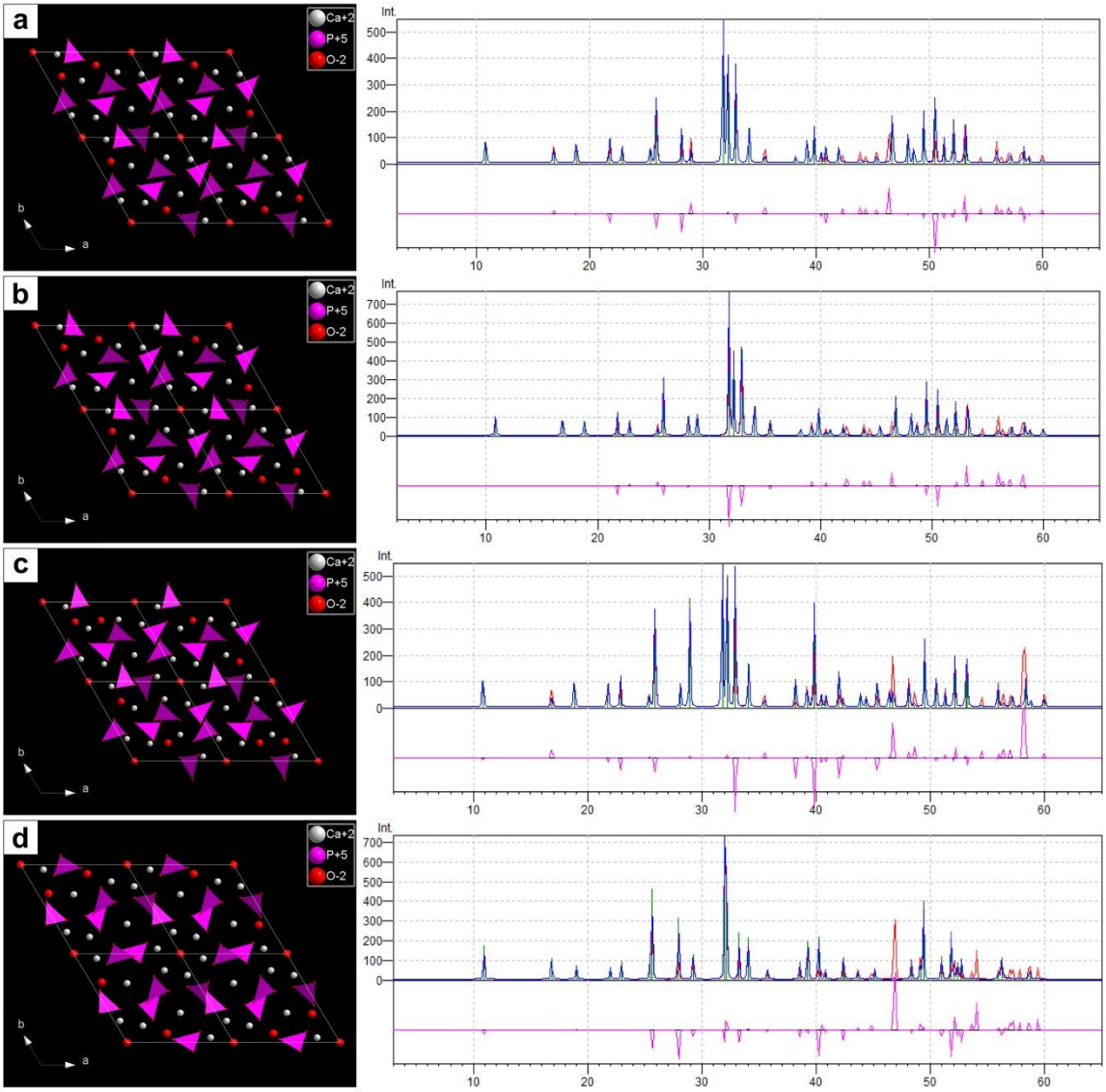

Figure 4, view of HA unit cell modeled along crystallographic "c" axis for **(a)** non-stoichiometric HA, **(b)** HA/MoO_x (II), **(c)** HA/MoO_x (III) and **(d)** HA/MoO_x (IV) samples. DRX comparison: (blue) theoretical XRD data, (red) experimental XRD data and (pink) match of theoretical and experimental XRD data; total correlation should give a straight line. Please refer to the web version of this article for interpretation of the color references.

Contraction of lattice parameters would be produced because the anion $(MoO_4)^{2-}$ presents a slightly reduction in its topological polar surface, ~ 80.3 $Å^2$ [37], compared to $(PO_4)^{3-}$, ~ 86.2 $Å^2$ [38]. The slightly increase of Ca/P elemental ratio along HA/MoO_x (I-II) samples derived

View Article Online
DOI: 10.1039/C9NR01236B

undoubtedly from a certain degree of P – Mo replacement into HA lattice. Furthermore, for those HA/MoO_x (III-IV) samples, which showed both powellite and HA diffraction patterns, the elemental Ca / Mo ratio, acquired on the spherical deposits, was about two, **figure ESI6-c**. This value is superior to that of stoichiometric powellite, Ca / Mo = 1, so we assumed that we were in the presence of a Ca^{2+} – rich powellite phase.[39] Modeled tetragonal unit cell and computed crystallographic parameters of powellite phase for the HA/MoO_x (III-IV) samples were comparable to standard values, please refer to section **ESI-2** and **table 1**. Knowing that Ca^{2+} was in an excess, **figure ESI6-c,** we assumed that nearly all the Mo atoms crystallized in a powellite structure form and the remaining Ca^{2+} would be trapped either in an amorphous form of $CaMoO_4$ or in an unknown calcium amorphous assembly.[8]

-please insert table 1, here-

HA/MoO_x platforms were found to be very sensitive to the synthesis conditions. We reasoned that differences among the final obtained specimens were due to PMA/nano-HA interaction in a precise pH reaction media that simultaneously influenced the formation processes of the molybdate anions[40] and the mechanisms of dissolution of HA nanoparticles.[41] Against the forecasts, those materials prepared with less amount of PMA (HA/MoOx (III) and HA/MoOx (IV)) resulted in an amalgam of powellite/HA phases, whereas those made with higher PMA/nano-HA ratio (HA/MoOx (I) and HA/MoO_x (II)) roused MoO_4-substituted HA. During the obtainment of HA/MoOx (I) and HA/MoO_x (II) samples, it was determined that the initial pH of PMA solutions was about 1.5 and, after the addition to the HA nanoparticles dispersions (pH = 9)[18, 28] it became to 2.3 and 3.4 for HA/MoOx (I) and HA/MoOx (II) respectively. In such conditions, nano-HA dissolution is highly favored and those effect is accelerated by the temperature intensification during the

View Article Online
DOI: 10.1039/C9NR01236B

hydrothermal treatment.[6, 8] There is little known about HA dissolution models and their validity under strong inorganic acid solutions (pH < 2, and T > 70 °C[41]). However, there is a general agreement that dissolution progresses under the following stages: (i) diffusion of chemical reagents (H^+, acid anions) from bulk solution to the solid/liquid interface; (ii) adsorption of chemical reagents onto the apatitic surface; (iii) surface chemical transformation; (iv) desorption of apatitic products (F^-, Ca^{2+} and PO_4^{-3}) and (v) diffusion into the bulk solution. An analysis by UV-vis spectrophotometry of the reaction medium at the end of the synthesis revealed two peaks around 215 and 310 nm characteristics of the intact Keggin's structure oligomolybdate anions[42], **figure ESI7**. This finding was in agreement with the formation of highly soluble calcium-phosphomolybdate complexes between the phosphomolybdic anions from PMA and the Ca^{2+} ions extracted from HA.[42]

Despite extreme reaction conditions, HA nanoparticles were partially dissolved, probably due to an extra stabilization of their structure by replacement of the extracted orthophosphate ions, PO_4^{-3}, by MoO_4^{-2} in accord with the formation of a MoO_4-substituted HA crystal. A similar stabilization was obtained for Mg-substituted HA in a previous work.[8] The final amount of molybdenum incorporated into HA/MoOx (I) and HA/MoOx (II) materials was very small in contrast to those that were initially added, **table 1**. Almost 98 % of initially added Mo remained in solution. At this point, we have to expound that due to the high HA dissolution, a very little amount of HA/MoOx (I) specimen was collected. This fact and its physicochemical similarity to the HA/MoOx (II) sample, made it discarded in the future analysis.

On behalf of HA/MoOx (III) and HA/MoOx (IV) materials, which were synthesized with less concentrated PMA solutions (pH = 4.5), the pH media after integration of all reactants was about 7.5. In such conditions nano-HA are dissolved slowly[6] releasing Ca^{2+}, while the

View Article Online
DOI: 10.1039/C9NR01236B

formation of MoO_4^{2-} is favored.[40] Both facts supported the precipitation of powellite phase ($CaMoO_4$). Since the Mo/Ca molar ratio in powellite deposits agreed, relatively well, with the initially added amounts, **table 1**, it could be affirmed that the entire Mo precipitated as powellite, whether crystalline or amorphous.

Intrinsic point defects within HA/MoO$_x$ platforms: induction of self-activated fluorescence and redox responsiveness

In the previous section, we have demonstrated that, under definite reaction conditions, PMA introduced MoO_4^{2-} ions within the hydroxyapatite lattice (HA/MoOx (I-II)) or generated $CaMoO_4$ / HA merged materials (HA/MoOx (III-IV)). Throughout this process, intrinsic electronic point defects are created into the primary HA crystal. They will be responsible for the optoelectronic properties of the material and, as we will demonstrate at the end of this work, they will be crucial for their interactions with microorganisms.

The optical band gap energy (E_g) of the obtained HA and HA/MoO_x materials, was estimated by plotting $(\alpha h\nu)^m$ against the photon energy $(h\nu)$, as shown in **section ESI-4**. Non-treated HA and HA/MoO_x (II) samples presented E_g values of 5.868 ± 0.135 and 5.651 ± 0.211 eV respectively; about 2 ± 0.1 eV inferior than literature reported information for theoretical hexagonal defect-free HA (E_g = 7.7 ± 0.2 eV)[43,44]. However, the data matched to experimental values (E_g = 5. 5 eV)[45] reported for the OH- vacancy HA cell, in entirely agreement with the structure of our non-stoichiometric HA, $(Ca^{+2})_{9.12}(PO_4^{-3})_{5.12}(HPO_4^{-2})_{0.88}(OH^-)_{1.12}$. Exhibiting an E_g > 5.5 eV, the HA and HA/MoO_x (II) samples should be transparent to visible light and electronic excitations should be possible only under middle- or far-ultraviolet illumination, most probably with $h\nu_{EX}$ > 6 eV. Photoluminescent (PL)

View Article Online
DOI: 10.1039/C9NR01236B

patterns of HA and HA/MoO_x specimens at RT, are shown in **figures 5a-d**, primary PL emissions are summarized in **table 2**.

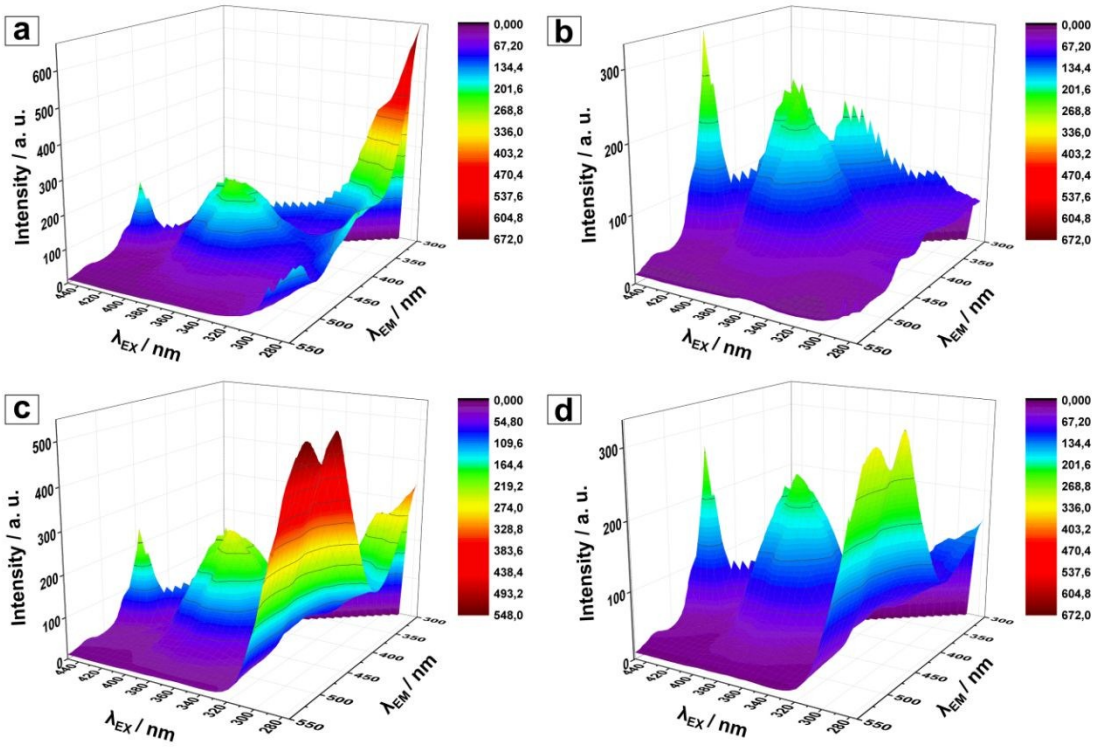

Figure 5, 3D photoluminescence (PL) excitation-emission patterns at RT of **(a)** HA, **(b)** HA/MoOx (II), **(c)** HA/MoOx (III) and **(d)** HA/MoOx (IV) samples. Please refer to the web version of this article for interpretation of the color references.

Highest emission of HA was detected at λ_{EM} = 310 nm (4.00 eV) after being exited with $h\nu_{EX}$ > 5 eV, **figure 5a**. The band gap energies increase straight with the structural order[46], so the requirement of excitation energy of about 1.5 eV inferior to the E_g implies that behind this effect we should have a transition involving at least one bound state located in the gap, most probably associated with defects. In the previous section, we have demonstrated that both HA and HA/MoO_x specimens presented distortions in their lattice and in their interatomic composition. These are associated to replacements, vacancies, inter-nodes and other defects[45] with a redistribution of the electrons in the occupied /

View Article Online
DOI: 10.1039/C9NR01236B

unoccupied electronic energy levels. This would shift the electronic levels (including shifts of the top of the valence band, E_v, the bottom of the conduction band, E_c, and hence the width of the forbidden energy zone, $E_g = E_c - E_v$), and would create new energy levels, E_i, inside the energy gap. The data obtained on the untreated HA-PL spectrum at RT suggested that there was a recombinant energy level in the forbidden band with a value of $E_i \approx 4.0$ eV (or 310 nm line) from the bottom of the conductance band.[45]

-please insert table 2, here-

Likewise, two lower intensity PL emissions corresponding to $E_i = 2.82$ and 2.69 eV levels could be observed, which gave the material a certain degree of blue epi-fluorescence and in a much lower proportion of a green epi-fluorescence, **figure 6**. On the basis of literature data, we assumed that the origin of these defects might be derived to the presence of both –OH vacancies (partially occupied interstitial –OH, $E_i \approx 2.75$ and 2.48 eV)[47] and H-internodes (interstitial, $E_i \approx 3.92$ eV).[45, 47] The incorporation of Mo^{6+} as MoO_4^{2-} into the HA structure along HA/MoOx (II) sample, induced the total disappearance of the peak associated with the H-internodes (4.0 eV), while preserved the peaks related to the -OH vacancies, $E_i \approx$ 2.69 and 3.00 eV. The presence of the metal point defects would change both the emission quantum yield and the fluorescence lifetime[48], observing in this particular case, an amplified blue epi-fluorescence, **figure 6**. The HA/MoOx (III and IV) specimens, meanwhile, presented optical band gap values ($E_g = 4.77$ eV) lowered than those found in the untreated HA and in the HA/MoOx (II) sample; these values were associated to the presence of powellite phase ($E_g \approx 4.70$ eV[46]). PL-emissions at 2.69 eV and 3.00 eV (associated to the presence of –OH vacancies) were maintained, although the most relevant PL- emissions of these samples occurred at $\lambda_{EM} = 523$ nm and $\lambda_{EM} = 473$ nm ($E_i = 2.37$ and

View Article Online
DOI: 10.1039/C9NR01236B

2.62 eV). In agreement with the literature information[46], PL-profiles, **figures 5c-d**, were typical of a multi-phonon and multi-level process, that is, a system in which relaxation occurs by several paths, involving the participation of numerous states within the band gap of the material.

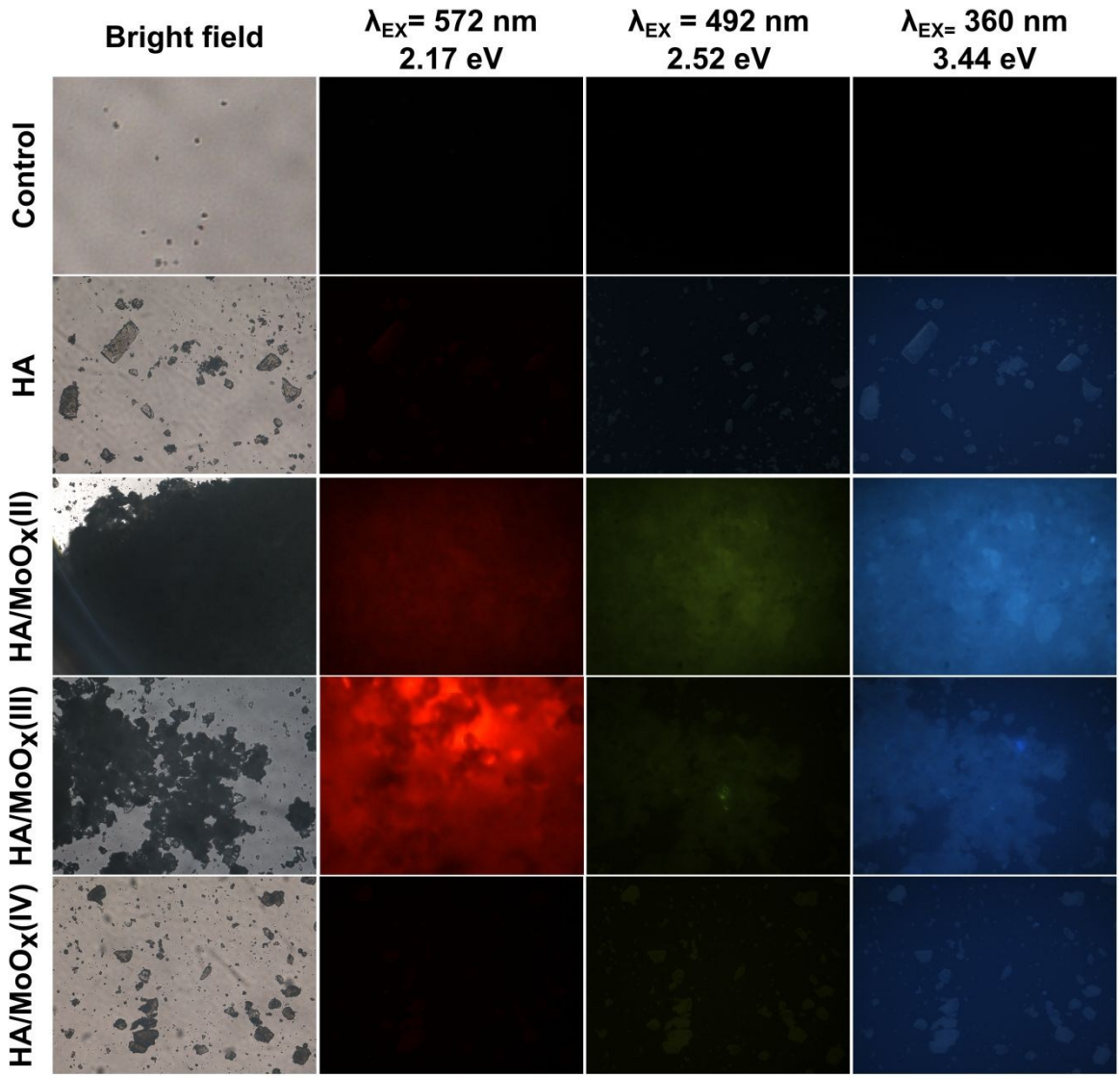

Figure 6, Epifluorescence microscope images of HA and HA/MoO_x materials at RT. Uncoated wells were used as control (**C**). Please refer to the web version of this article for interpretation of the color references.

View Article Online
DOI: 10.1039/C9NR01236B

Both samples showed red epi-fluorescence, being more intense for the HA/MoOx (III) specimen, **figure 6**. In addition, the interference of new electronic levels at E_i = 2.37 and 2.62 eV with the -OH vacancies reduced blue epi-fluorescence.

Disruption of electronic levels, additionally, can drive to variations in surface charges.[45] In this regard, surface ζ-potential of all samples were measured, **section ESI-9**, and shown in **table 2**. Obtained data were similar to those reported in literature and in our previous works[10, 28]; we did not find any evidence of the surface charge alteration due to MoO_4^{-2} – PO_4^{-3} substitution or to HA / $Ca(MoO_4)$ merge.

The –OH vacancy influence is very important, because not only they affect E_g values, but also they create trapping electrons levels from the conduction band in the middle of the forbidden zone.[47] The formation of this type of defects would be related to the ability of a material to accept electrons and, therefore, would regulate its redox responsiveness. Knowing that cell's internal processes involve reduction-oxidation (redox) reactions and that redox potential is well recognized as a regulatory factor of cellular activities[49], the biological redox status of nano-HA/MoO_x platforms was analyzed. The samples were contrasted against L-ascorbic acid (AA) redox probe to evaluated their redox potential (redox intensity component) and the pool of electrons able to be transferred (redox capacity component). Cyclic voltammetry curves obtained for the nano-HA/MoO_x modified-GC electrodes at 50 mV s^{-1} are shown in **figure 7a**. At the operational conditions, AA always displayed its characteristic single oxidation peak at the potential region between 0.0 and 0.8 V, demonstrating that all tested materials acted as electron acceptors. It was observed that the anodic peak, consistent to the irreversible electrochemical transformation of AA into dehydroascorbic acid[26], increased with the presence of Mo. The maximum values

View Article Online
DOI: 10.1039/C9NR01236B

corresponded to HA/MoO_x (III) and HA/MoO_x (IV) samples, while as it was expected, the HA/MoO_x (II) specimen with a less content of Mo combined to the HA structure showed the minimum value.

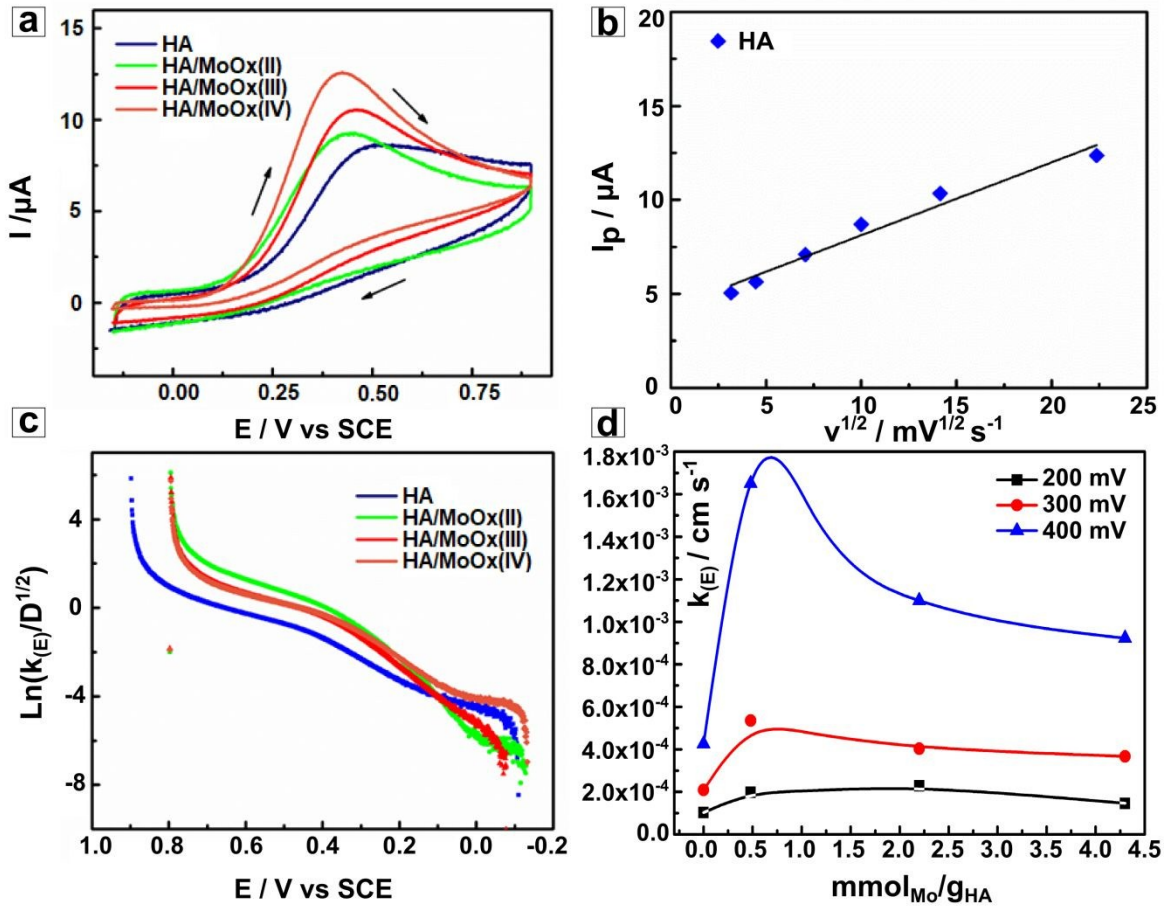

Figure 7, **(a)** steady cyclic voltammetry (CV) curves of modified-GC electrodes in 10 mM AA PBS solution (pH = 7.2) at a scan rate of 100 mV s^{-1}. The arrows indicate the scan direction. **(b)** Randles−Ševčik plot obtained from the CV data for the unmodified HA electrode; scan rates ranging from 10 to 500 mV s^{-1}. **(c)** Semi-integral cyclic voltammogram (anodic branch) for the electro-oxidation of AA at the nano-HA/MoO_x modified-GC electrodes. **(d)** Variation of the apparent heterogeneous rate constant, $k_{(E)}$, as a function of the effective Mo quantity, E = 200, 300 and 400 mV. Please refer to the web version of this article for interpretation of the color references.

Nevertheless for all HA/MoO_x materials, the anodic peak potential (E_p) shifted gradually to less positive values after Mo - HA amalgamation compared to untreated HA electrode (E_p =

View Article Online
DOI: 10.1039/C9NR01236B

0.48 V). **Figure 7b** shows the Randles−Ševčik plot for untreated HA samples, a similar linearly correlation was obtained for HA/MoO_x samples. Linearly variation of the current peak with the square root of the scan rate over the entire inspected run confirmed that the irreversible oxidation processes of AA at all tested nano-HA/MoO_x modified-GC electrodes was regulated by a diffusion mechanism. According to this mechanism, the transference of the first electron from AA to form the ascorbyl radical anion is the rate-determining step (rds) of the reaction.[50] The apparent heterogeneous rate constant, $k_{(E)}$, was estimated from the semi-integral analysis of the anodic branch of the voltammograms, **figure 7c**; obtained values are summarized in **figure 7d**. It could be noted that $k_{(E)}$ was strongly influenced by the MoO_4^{2-} - PO_4^{3-} substitution and that responded to the intensity of the applied electric field (E). After the increment of the electric field's intensity, it was observed that $k_{(E)}$ acquired a maximum value for the HA/MoO_x (II) material, which contained no extra MoO_4^{2-} - crystalline phases. Since the effect of -OH vacancies were apparently increased in HA/MoOx (II) sample and this fact was, in turn, linked to the creation of electron entrapment levels, this also would explain the increase of $k_{(E)}$ in the AA electro-oxidation reaction, **figure 7d**. HA/MoO_x (III) and HA/MoO_x (IV) specimens composed by a blend of hydroxyapatite and powellita phases, showed similar $k_{(E)}$ values at all E. Note that $k_{(E)}$ decreased in the HA/MoOx (III and IV) samples, **figure 7d**, as well as their blue epi-fluorescence, **figure 6**; both facts were associated to the reduction of -OH vacancies influence.

Targeting of nano-HA/MoO_x platforms antimicrobial activity

In several works, we have established the biocompatibility of our synthesized rod-like HA nanoparticles and their bone repair capacity.[6-8, 10, 28] Nevertheless, as was previously

View Article Online
DOI: 10.1039/C9NR01236B

exposed, the presence of molybdenum alters their chemical composition, morphology, crystalline degree, crystallographic unit cell parameters and electronic defects, which can lead to potential toxicity. Thus, before proceeding, nano-HA/MoO_x platforms harmlessness was verified after 24 and 48 h of contact with rOBs primary cells.

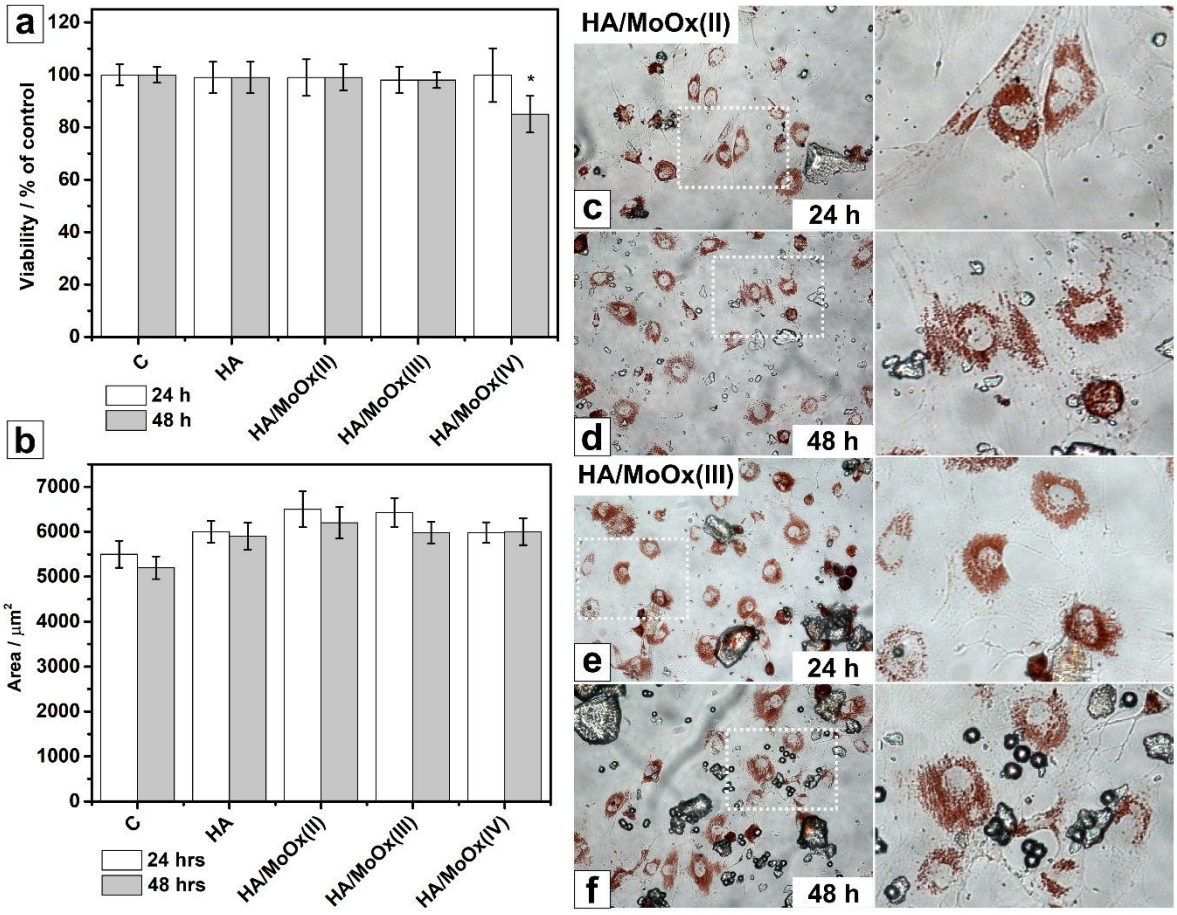

Figure 8, **(a)** rat primary osteoblast (rOBs) viability and **(b)** spreader cellular area after 24 and 48 hrs of culture in the presence of nano-HA/MoO_x platforms. Results were expressed as percentages relative to the control (C). **(c-f)** Representative optical photographs of adhered rOBs stained with Neutral Red dye after 24 - 48 h of culture.

Osteoblasts are crucial to the expansion, growth, function, repair and maintenance of bone host tissue[51] and nano-HA/MoO_x materials are proposed as novel platforms for bone tissue repair, then it is essential to verify their biocompatibility in the presence of this type of

View Article Online
DOI: 10.1039/C9NR01236B

cells. The ability of cells to assimilate dye molecules into their lysosomes was examined by Neutral Red assay; only viable cells are capable to complete this effort, so lisosomal activity is considered as an indirectly quantification of cell viability.[29]

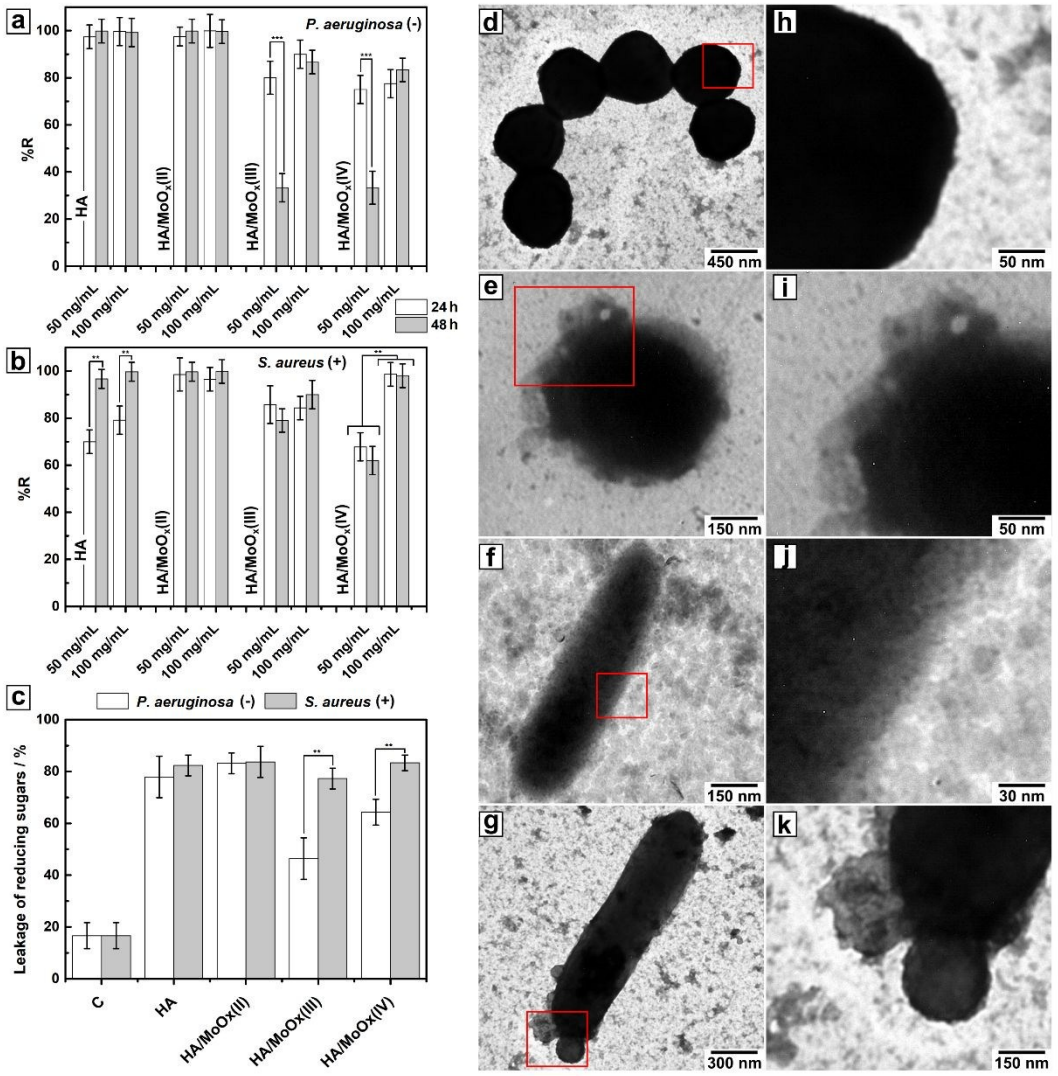

Figure 9, Antibacterial activity of HA/MoO_x powders against **(a)** *P. aeruginosa* and **(b)** *S. aureus* as a function of material concentration; contact: 24 and 48 h. Results are expressed as reduction percentage (R %). **(c)** Leakage of reducing sugars after 48 h of bacterial contact with 100 mg / mL of different HA/MoO_x powders; bacteria cultured without the material presence was used as control, C. Asterisks denote statistically significant differences (**$p < 0.01$, ***$p < 0.001$); significant differences between the samples are indicated with brackets. TEM microphotographs of *S. aureus* after cultured alone **(d, h)** and in the presence of HA/MoO_x (II) sample **(e, i)**. TEM microphotographs of *P. aeruginosa* after cultured alone **(f, j)** and in the presence of HA/MoO_x (II) sample **(g, k)**.

View Article Online
DOI: 10.1039/C9NR01236B

Obtained results, **figure 8a**, showed that lysosome activity of rOBs cultured after 24 and 48 h in the presence of HA/MoO_x platforms had no statistically significant differences respect to control, C, or to untreated HA sample. Although it could be appreciated a slight reduction of lysosome activity after 48 h of culture in the presence of HA/MoOx (IV), it was not found to be significant with respect to the other samples and for this reason was considered negligible. Cellular active proliferation status was confirmed by optical microscopic observations. Primary rOBs always exhibited their characteristic polygonal, stretched, and flat shape morphology tightly adhered to the surface; no statistically significant differences on spreader area could be appreciated compared to control, **figures 8b-f**.

After the biocompatibility of the HA/MoO_x platforms was confirmed, their antibacterial activity was analyzed. **Figures 9a-b** show the proliferation reduction percentage of Gram-positive (*S. aureus*) and Gram-negative (*P. aeruginosa*) bacteria after 24 - 48 h of incubation in the presence of untreated HA and HA/MoO_x samples. All tested materials displayed an R % ≈ 100 at a concentration of 100 mg/ mL after 48 h of contact against all studied microorganisms without any statistically difference. HA/MoOx (II) sample also exerted a complete antibacterial activity at 50 mg / mL against both strains after 24 and 48 h of exposition. The effect of HA/MoOx (II) material was slightly superior to untreated HA sample against Gram-positive bacteria because pure HA showed only a 80 % of bacterial proliferation reduction after 24 h of treatment at all tested concentrations. HA/MoOx (III-IV) specimens displayed a clear reduction of their antibacterial activity at a 50 mg / mL concentration after 48 h of treatment against *P. aeruginosa* (R % ≈ 34). This effect was also evidenced, but in lower magnification, against Gram-positive strain; in this last situation

View Article Online
DOI: 10.1039/C9NR01236B

merely HA/MoOx (IV) specimen experimented a reduction of its antibacterial activity and the effect was similar to those observed for the untreated HA sample. The analysis of the obtained data, **figures 9a-b**, revealed that even if there was a connection between bacterial reduction and the presence of molybdenum within HA lattice, there was not a linear correlation with its amount. To analyze the obtained results, we must take into account that a system with possible antibacterial properties can exerts an action on at least one of the following key points affecting the microorganism survival: (i) microenvironment, (ii) adhesion, and (iii) metabolic state.[9] The first effect to be analyzed was the influence of HA/MoO_x platforms on the microbial culture media. In accordance with HA and powellite phases solubility products at 37°C and 1 bar, $pK_{SP}^{HA} = -\log\left(K_{SP}^{0,HA}\right) = 54.86$ and $pK_{SP}^{pow} = -\log\left(K_{SP}^{0,pow}\right) = 8.44$, [52] both untreated HA and HA/MoO_x derivatives behave as insoluble salts under physiological conditions. However, the structural base of all materials, HA nanoparticles, are designed to be biodegradable[6, 8], so they can release a degree of ionic concentrations, affect the physical and chemical properties of broth, and consequently, the optimum media conditions of bacteria evolution. The release of $[OH^-]$ = 0.47 mM, $[PO_4^{-3}]$ = 2.14 mM, $[HPO_4^{-2}]$ = 0.37 mM and $[MoO_4^{-2}] < 1$ μM ions slightly alkalized the broth, **section ESI-10**. After material incorporation, the pH value of bacterial nutritive culture broth raised a maximum value of 8.1 ± 0.2 in all cases, which is conductive to bacterial burden.[53] Regarding to the ionic concentrations, it was confirmed during the bio-compatibility tests that the solubilized ionic amounts were within the non-toxicity range[9] and, were not enough to exert an action on the water availability by restraining its accessibility to organisms.[54] Therefore, it cannot be associated with the

View Article Online
DOI: 10.1039/C9NR01236B

experimental results summarized in f**igures 9a-b**, where a clear antibacterial effect was evidenced.

Because of the difference between the surface energy of bacteria and the broth in which they are suspended, cells preferentially attach to lower-surface-energy substrates. The next point to be considered is related to microorganism – material surface interaction; here the surface charge plays a distinctive role. It was well established that the use of cationic substances disturbs the surface negativity (ζ- potential) of microorganisms membrane by an alteration of lipid mediated signaling and eventually conduce to a membrane destabilization followed by death.[55] *S. aureus* and *P. aeruginosa* possesses ζ- potential values of about -35.6, and -14.4 mV[9] respectively; being electronegative it may be expected some degree of electrostatic repulsion between microorganisms and the negatively charged material surfaces, **table 2**. The obtained results did not evidence a direct correlation between the materials surface charge and the reduction of bacterial proliferation. Therefore, in terms of electrostatic cues, there was not an effect of HA and HA/MoO_x samples against bacteria progression.

The final step in our work led to connect the HA and HA/MoO_x samples electronic properties with bacterial reduction and, consequently, to analyze their capacity to influence the redox mechanism by which the electron-transport chain enables prokaryote cells to generate the energy that they need to survive. Examining the variation of the electron apparent heterogeneous rate constant, $k_{(E)}$, it could be observed that the sample HA/MoOx (II) which exhibited the maximum $k_{(E)}$ value also displayed the greatest and fastest bacterial reduction ability at all tested concentrations and against both Gram-negative and Gram-positive strains. Untreated HA and HA/MoO_x (III and IV) samples also exhibited electron acceptor capacity, **figure 5d**, but their kinetic constants were less significant so their

View Article Online
DOI: 10.1039/C9NR01236B

antibacterial effect required further time. In this situation, microorganisms would have enough time to recover their population; note that after 48 h of treatment the R % decreased, **figure 9a-b**. The increment of $k_{(E)}$, was maximum after MoO_4^{2-} - PO_4^{3-} substitution into the HA crystal lattice and the creation of –OH vacancies. Untreated HA, exerted a similar antibacterial activity than HA/MoO_x (II) sample and a slightly superior effect than HA/MoO_x (III-IV) specimens, which was in agreement with the presence of –OH vacancies and electrons acceptor abilities. As it was demonstrated in the previous section, the MoO_4^{2-} - PO_4^{3-} substitution in HA/MoO_x (II) sample potentiated the effect of –OH vacancies reducing the H-interstitial nodes. HA / powellite combinations (HA/MoO_x (III-IV) samples), on the other hand, also displays higher –OH vacancies to accept electrons from bacteria than untreated HA, however their effect was slightly reduced or altered for the presence of defects at E_i = 2.37 and 2.62 eV. The reduction of electronic defects in HA/MoO_x (III-IV) samples was in harmony with the decrease of their antibiotic abilities compared to their counterparts: untreated HA and HA/MoO_x (II).

Metabolic electronic transference of prokaryotic cells occurs through its cytoplasmic membrane; therefore, microorganism annihilation can be associated to the disturbance and rupture of it. If this was the case, a leakage of cytoplasmic constituents ought to occur, for example the leakage of reducing sugars. **Figure 9c** revealed that HA and HA/MoO_x platforms boosted the leakage of reducing sugars from cytoplasmic membrane. Almost no reducing sugars leakage could be detected in control experiments, while the escape amount of reducing sugars from treated cells well correlated to R % values, **figures 9a-b**. Membrane rupture was confirmed by TEM inspection, **figures 9d-9k**. Compared with control cells, treated bacteria showed a loss of material through their inner capsular layers.

View Article Online
DOI: 10.1039/C9NR01236B

Bacterial extermination mechanism associated to extracellular electron transfer, EET, was in reasonably agreement with literature information and with our previously obtained results.[9, 56] We can hypothesize that electronic transfer to HA/MoO_x platforms did not affect eukaryote cells because of the compartmentation of metabolism within mitochondria; for this reason, as we have demonstrated, the materials were always biocompatible, **figure 8**.

Conclusion

Here we have exposed the effect of molybdenum (Mo) assimilation within the crystalline lattice and in the electronic configuration of bone mimetic hydroxyapatite (non-stoichiometric calcium deficient hydroxyapatite, HA). Mo incorporation into HA is subject to the synthetic conditions that straight influence the final properties of materials. Through a delicate control of the reaction conditions, it was possible to obtain biocompatible materials that simultaneously exhibited blue and red self-activated fluorescence at room temperature and antibacterial activity. The best performance of multifunction integration was obtained from HA/MoO_x(II) and HA/MoO_x(III) specimens. It was determined that optoelectronic and antibacterial skills had their origin in the generation and modulation of the electronic defects within HA crystal; specifically they were associated to –OH group vacancies that acted as electron acceptor centers. Electronic centers were originally detected in untreated HA, but their effect was intensified after MoO_4^{2-} - PO_4^{3-} substitution (HA/MoO_x(II)) and to a lesser extent after the amalgamation with powellite phase (HA/MoO_x(III)).

Our results validate the importance of electronic transference properties through biomaterials that, as far as our knowledge, they are slightly considered in the implant

View Article Online
DOI: 10.1039/C9NR01236B

designs. From here, new paths towards the development of multifunctional platforms that can be used to drive innovative bone repair strategies are opened.

Acknowledgements: The authors acknowledge the financial support of Universidad Nacional del Sur (UNS, PGI 24/Q092), Concejo Nacional de Investigaciones Científicas y Técnicas (CONICET, PIP – 11220130100100CO), Agencia Nacional de Promoción Científica y Tecnológica (ANPCyT, PICT 201-0126) Argentina; and Xunta de Galicia (AEMAT, ED431E2018/08 and ED431B2017/21), Spain. DP and JAL have fellowships of CONICET. JMS, GES and PVM are researchers of CONICET.

Electronic supplementary information (ESI) available: It contains additional information of the crystallographic parameters and molecular modeling resolution; cyclic voltammetry study and optoelectronic properties determination; biocompatibility assays; nanoparticles size distribution histograms, elemental microanalysis and processing, ζ-potential and *in vitro* hydrolytic degradation measurements.

View Article Online
DOI: 10.1039/C9NR01236B

References

1. National Institutes of Health, ed., *Understanding emerging and re-emerging infectious diseases*, 2007.
2. M. Ribeiro, F. J. Monteiro and M. P. Ferraz, *Biomatter*, 2012, **2**, 176-194.
3. J. A. Inzana, R. P. Trombetta, E. M. Schwarz, S. L. Kates and H. A. Awad, *Eur. Cells Mater.*, 2015, **30**, 232.
4. V. Uskoković and T. A. Desai, *Expert Opin. Drug Deliv.*, 2014, **11**, 1899-1912.
5. J. S. Gogia, J. P. Meehan, P. E. Di Cesare and A. A. Jamali, Local antibiotic therapy in osteomyelitis, 2009.
6. N. L. D'Elia, C. Mathieu, C. D. Hoemann, J. A. Laiuppa, G. E. Santillan and P. V. Messina, *Nanoscale*, 2015, **7**, 18751-18762.
7. J. Sartuqui, C. Gardin, L. Ferroni, B. Zavan and P. V. Messina, *Mater. Today Commun.*, 2018, **16**, 152-163.
8. N. C. Andrés, N. L. D'Elía, J. M. Ruso, A. E. Campelo, V. L. Massheimer and P. V. Messina, *ACS Appl. Mater. Interfaces*, 2017, **9**, 15698-15710.
9. N. C. Andrés, J. M. Sieben, M. Baldini, C. H. Rodríguez, Á. Famiglietti and P. V. Messina, *ACS Appl. Mater. Interfaces*, 2018, **10**, 19534-19544.
10. D. Placente, L. A. Benedini, M. Baldini, J. A. Laiuppa, G. E. Santillán and P. V. Messina, *Inter. J. Pharm.*, 2018, **548**, 559-570.
11. R. R. Mendel and F. Bittner, *Biochim. Biophys. Acta, Mol. Cell Res.*, 2006, **1763**, 621-635.
12. I. A. de Castro, R. S. Datta, J. Z. Ou, A. Castellanos-Gomez, S. Sriram, T. Daeneke and K. Kalantar-zadeh, *Adv. Mater.*, 2017, **29**, 1701619.
13. A. M. Ribeiro, T. H. Flores-Sahagun and R. C. Paredes, *J. Mater. Sci.*, 2016, **51**, 2806-2816.
14. K. Krishnamoorthy, M. Veerapandian, K. Yun and S. J. Kim, *Colloids Surf. B,* 2013, **112**, 521-524.
15. R. K. Singh, T.-H. Kim, C. Mahapatra, K. D. Patel and H.-W. Kim, *Langmuir*, 2015, **31**, 11344-11352.
16. K. Deshmukh, M. M. Shaik, S. R. Ramanan and M. Kowshik, *ACS Biomater. Sci. Eng.*, 2016, **2**, 1257-1264.
17. ASTM International, West Conshohocken, PA, , 2016.
18. F. Ye, H. Guo, H. Zhang and X. He, *Acta Biomater.*, 2010, **6**, 2212-2218.
19. J. R. A. Sietsma, A. Jos van Dillen, P. E. de Jongh and K. P. de Jong, in *Studies in Surface Science and Catalysis*, eds. E. M. Gaigneaux, M. Devillers, D. E. De Vos, S. Hermans, P. A. Jacobs, J. A. Martens and P. Ruiz, Elsevier, 2006, vol. 162, pp. 95-102.
20. C. A. Schneider, W. S. Rasband and K. W. Eliceiri, *Nat. Methods*, 2012, **9**, 671.
21. B. Lafuente, R. T. Downs, H. Yang and N. Stone, in *Highlights in Mineralogical Crystallography*, ed. T. a. R. M. D. Armbruster, R.M. , De Gruyter, W, Berlin, Germany, Armbruster, T and Danisi, R M edn., 2015, pp. 1-30.
22. B. A. Hunter, Rietica - a visual Rietveld program, Australia, 2000.
23. H. Putz, J. Schön and M. Jansen, *J. Appl. Crystallogr.*, 1999, **32**, 864-870.
24. J. Hrbac, V. Halouzka, L. Trnkova and J. Vacek, *Sensors*, 2014, **14**, 13943.
25. A. J. Bard and L. R. Faulkner, John Wiley, 2001.
26. M. R. Deakin, P. M. Kovach, K. J. Stutts and R. M. Wightman, *Anal. Chem.*, 1986, **58**, 1474-1480.
27. J. Tauc and A. Menth, *J. Non-Cryst. Solids*, 1972, **8**, 569-585.
28. N. L. D'Elía, A. N. Gravina, J. M. Ruso, J. A. Laiuppa, G. E. Santillán and P. V. Messina, *Biochim. Biophys. Acta, Gen. Subj.*, 2013, **1830**, 5014-5026.

View Article Online
DOI: 10.1039/C9NR01236B

29. G. Repetto, A. del Peso and J. L. Zurita, *Nat. Protoc.*, 2008, **3**, 1125.
30. S. Foldberg, M. Petersen, P. Fojan, L. Gurevich, T. Fink, C. P. Pennisi and V. Zachar, *Colloids Surf. B,* 2012, **93**, 92-99.
31. A. A. Miles, S. S. Misra and J. O. Irwin, *J. Hyg.*, 1938, **38**, 732-749.
32. A. Mattson and C. Jensen, *Anal. Chem.*, 1950, **22**, 182-185.
33. D. Ellis, J. Terra, O. Warschkow, M. Jiang, G. B. González, J. Okasinski, M. Bedzyk, A. M. Rossi and J.-G. Eon, *Phys. Chem. Chem. Phys.*, 2006, **8**, 967-976.
34. J. M. Ruso, V. Pardo, J. Sartuqui, N. Gravina, N. L. D'Elía, O. I. Pieroni and P. V. Messina, *ACS Appl. Mater. Interfaces*, 2015, **7**, 12740-12750.
35. N. Gravina, J. M. Ruso, D. A. Mbeh, L. H. Yahia, Y. Merhi, J. Sartuqui and P. V. Messina, *RSC Adv.*, 2015, **5**, 8077-8087.
36. C. Meneghini, M. C. Dalconi, S. Nuzzo, S. Mobilio and R. H. Wenk, *Biophys. J.*, 2003, **84**, 2021-2029.
37. National Center for Biotechnology Information, PubChem Compound Database; CID = 24621, https://pubchem.ncbi.nlm.nih.gov/compound/molybdate.
38. National Center for Biotechnology Information, PubChem Compound Database; CID = 1061, https://pubchem.ncbi.nlm.nih.gov/compound/1061.
39. J. V. Crum, J. J. Neeway, B. J. Riley, Z. Zhu, M. J. Olszta and M. Tang, *J. Nucl. Mater.*, 2016, **482**, 1-11.
40. H. Wan, W. Yang, W. Cao, T. He, Y. Liu, J. Yang, L. Guo and Y. Peng, *Minerals*, 2017, **7**, 141.
41. S. V. Dorozhkin, *World J. Methodol.,* 2012, **2**, 1.
42. J. Javidi, M. Esmaeilpour, Z. Rahiminezhad and F. N. Dodeji, *J. Cluster Sci.*, 2014, **25**, 1511-1524.
43. M. Corno, C. Busco, B. Civalleri and P. Ugliengo, *Phys. Chem. Chem. Phys.*, 2006, **8**, 2464-2472.
44. L. A. Avakyan, E. V. Paramonova, J. Coutinho, S. Öberg, V. S. Bystrov and L. A. Bugaev, *J. Chem. Phys.*, 2018, **148**, 154706.
45. A. Bystrova, Y. D. Dekhtyar, A. Popov, J. Coutinho and V. Bystrov, *Ferroelectrics*, 2015, **475**, 135-147.
46. J.-W. Yoon, C.-J. Choi and D. Kim, *Mater. Trans.*, 2011, **52**, 768-771.
47. V. Bystrov, J. Coutinho, A. Bystrova, Y. D. Dekhtyar, R. Pullar, A. Poronin, E. Palcevskis, A. Dindune, B. Alkan and C. Durucan, *J. Phys.D, Appl. Phys.*, 2015, **48**, 195302.
48. Z. Gryczynski, J. Malicka, I. Gryczynski, E. Matveeva, C. D. Geddes, K. Aslan and J. R. Lakowicz, *Proc. SPIE Int. Soc. Opt. Eng*., 2004, **5321**, 275-282.
49. Y. Hatori, S. Inouye, R. Akagi and T. Seyama, *Redox Biol.*, 2017, **14**, 679-685.
50. I. F. Hu and T. Kuwana, *Anal. Chem.*, 1986, **58**, 3235-3239.
51. P. Jayakumar, L. Di Silvio, K. E. Tanner and M. J. Dalby, *Proc. Inst. Mech. Eng., Part H,* 2010, **224**, 1415-1440.
52. T. P. Dadze, G. A. Kashirtseva, M. P. Novikov and A. V. Plyasunov, *Monatsh. Chem.*, 2018, **149**, 261-282.
53. L. Bennison, C. Miller, R. Summers, A. Minnis, G. Sussman and W. McGuiness, *Wound Practice & Research: Journal of the Australian Wound Management Association*, 2017, **25**, 63.
54. W. M. Sattley and M. T. Madigan, *eLS*, 2001, 1-10.
55. S. Halder, K. K. Yadav, R. Sarkar, S. Mukherjee, P. Saha, S. Haldar, S. Karmakar and T. Sen, *SpringerPlus*, 2015, **4**, 672-672.
56. G. Wang, H. Feng, A. Gao, Q. Hao, W. Jin, X. Peng, W. Li, G. Wu and P. K. Chu, *ACS Appl. Mater. Interfaces*, 2016, **8**, 24509-24516.

Table 1. Crystallographic parameters of nano-HA / MoO_x platforms. (*) Computed from the amounts of Ca^{2+} and Mo^{+6} added to the initial material synthesis solutions. (^{EDX}) Computed by EDX−Microanalysis results (figure ESI6).

	$Ca_{10}(PO_4)_6(OH)_2$ (JCPDS 9-436)	R130713.9	$Ca(MoO_4)$ R100180	HA	Samples / HA: $(Ca^{+2})_{9.12}(PO_4^{-3})_{5.12}(HPO_4^{-2})_{0.88}(OH^-)_{1.12}$ HA / MoOx (I)	HA / MoOx (II)	HA / MoOx (III)	HA / MoOx (IV)
PMA/nano-HA wt. ratio	---	---	---	---	4/1	2/1	1/1	1/2
Mo/Ca molar ratio(*)	---	---	---	---	2.17	1.07	0.54	0.26
Mo/Ca molar ratio (EDX)	---	---	---	---	0.05	0.05	0.45	0.23
				Hydroxyapatite phase				
$X_{c,HA}$ eq.(5, SM-1)	1	1	1	0.51	0.50	0.50	0.42	0.37
$X_{c,HA}$, eq. (6, SM-1)	1	1	1	0.50	0.48	0.48	0.41	0.35
$d_{(002)}$ / Å	3.441	3.456	---	3.457	3.455	3.449	3.447	3.445
$d_{(300)}$ / Å	2.719	2.725	---	2.725	2.722	2.719	2.713	2.711
a = b / Å	9.418	9.438	---	9.439	9.429	9.421	9.398	9.391
c / Å	6.881	6.911	---	6.914	6.910	6.898	6.894	6.890
V / Å^3	528.6	533.1	---	533.5	532.0	530.2	527.3	526.2
				Powellite phase				
$d_{(101)}$ / Å	---	---	4.764	---	---	---	4.751	4.763
$d_{(112)}$ / Å	---	---	3.111	---	---	---	3.105	3.109
a = b / Å	---	---	5.239	---	---	---	5.217	5.239
c / Å	---	---	11.457	---	---	---	11.502	11.434
V / Å^3	---	---	314.49	---	---	---	313.03	313.86

Table 2. Highest PL emissions, optical band gap energy (E_g) and surface ζ-potential for HA and HA/MoO_x specimens.

	Photoluminescence		ζ- potential / mV	E_g / eV
	λ_{EX} / nm; hν/ eV	λ_{EM} / nm; hν/ eV		
HA	440; 2.82 372; 3.33 280; 4.42	460; 2.69 439; 2.82 310; 4.00	-19.8 ± 1.9	5.868 ± 0.135
HA / MoOx (II)	440; 2.82 391; 3.17 362.5; 3.42	460; 2.69 411; 3.02 382; 3.24	-18.3 ± 0.9	5.651 ± 0.211
HA / MoOx (III)	440; 2.82 372; 3.33 280; 4.42	460; 2.69 436; 2.84 522; 2.37 477; 2.60	-17.0 ± 0.9	4.777 ± 0. 145
HA / MoOx (IV)	440; 2.82 372; 3.33 280; 4.42	460; 2.69 439; 2.82 523; 2.37 473; 2.62	-22. 3 ± 0.4	4.771 ± 0.109

View Article Online
DOI: 10.1039/C9NR01236B

Table of Content Entry

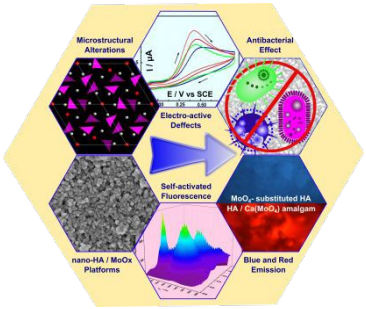

Unusual intrinsic electronic point defects of bone-mimetic hydroxyapatite nanoparticles induce a self-activated fluorescence and provoke pathogen microorganisms' death after its direct contact.